Published in final edited form as:

Cancer Discov. 2020 June ; 10(6): 806–821. doi:10.1158/2159-8290.CD-19-1330.

Mutations in the RNA splicing factor SF3B1 promote tumorigenesis through MYC stabilization

Zhaoqi Liu[1,2], **Akihide Yoshimi**[3], **Jiguang Wang**[4], **Hana Cho**[3], **Stanley Chun-Wei Lee**[3], **Michelle Ki**[3], **Lillian Bitner**[3], **Timothy Chu**[1,2], **Harshal Shah**[3], **Bo Liu**[3], **Anthony R. Mato**[5], **Peter Ruvolo**[6], **Giulia Fabbri**[7], **Laura Pasqualucci**[7,8], **Omar Abdel-Wahab**[3,5], **Raul Rabadan**[1,2]

[1]Program for Mathematical Genomics, Columbia University, New York, NY, USA

[2]Departments of Systems Biology and Biomedical Informatics, Columbia University, New York, NY, USA

[3]Human Oncology and Pathogenesis Program, Memorial Sloan Kettering Cancer Center, New York, NY, USA

[4]Division of Life Science, Department of Chemical and Biological Engineering, Center for Systems Biology and Human Health and State Key Laboratory of Molecular Neuroscience, The Hong Kong University of Science and Technology, Hong Kong SAR, China

[5]Leukemia Service, Department of Medicine, Memorial Sloan Kettering Cancer Center, New York, NY, USA

[6]Department of Leukemia, Division of Cancer Medicine, The University of Texas MD Anderson Cancer Center, Houston, TX, USA

[7]Institute for Cancer Genetics, and the Herbert Irving Comprehensive Cancer Center, Columbia University, New York, NY, USA

Corresponding Authors: Akihide Yoshimi, Memorial Sloan Kettering Cancer Center, Zuckerman Research Building, 417 E. 68th Street, New York, NY 10065, Phone: 646-888-3242; Fax: 646-422-0890; yoshimia@mskcc.org; Raul Rabadan, Columbia University Irving Medical Center 622 West 168th Street, PH18-200, New York, NY 10032, Phone: 212-305-3896; Fax: 212-851-5149; rr2579@cumc.columbia.edu.

Z. Liu, and A. Yoshimi share first authorship of this article.

Authors' Contributions

Conception and design: Z. Liu, A. Yoshimi, O. Abdel-Wahab, R. Rabadan

Development of methodology: Z. Liu, A. Yoshimi, O. Abdel-Wahab, R. Rabadan

Acquisition of data (provided animals, acquired and managed patients, provided facilities, etc.): Z. Liu, A. Yoshimi, H. Cho, S. C-W. Lee, M. Ki, L. Bitner, B. Liu, H. Shah, A. R. Mato, O. Abdel-Wahab

Analysis and interpretation of data (e.g., statistical analysis, biostatistics, computational analysis): Z. Liu, A. Yoshimi, J. Wang, R. Rabadan

Writing, review, and/or revision of the manuscript: Z. Liu, A. Yoshimi, O. Abdel-Wahab, R. Rabadan

Administrative, technical, or material support (i.e., reporting or organizing data, constructing databases): T. Chu, P. Ruvolo, G. Fabbri, L. Pasqualucci

Study supervision: O. Abdel-Wahab, R. Rabadan

A conflict of interest disclosure statement: A.R. Mato has received research funding from TG Therapeutics, AbbVie, Sunesis, LOXO, Pharmaacyclics/J&J, Regeneron, and DTRM BioPharma and has received consulting fees from TG Therapeutics, AbbVie, Acerta, Sunesis, LOXO, Pharmacyclics/J&J, Regeneron, Celgene, and Prime Oncology, all of which are unrelated to the current manuscript. O. Abdel-Wahab has served as a consultant for H3B Biomedicine, Foundation Medicine Inc, Merck, and Janssen, and is on the Scientific Advisory Board of Envisagenics Inc; O. Abdel-Wahab has received prior research funding from H3B Biomedicine unrelated to the current manuscript. R.R. is a consultant for AimedBio in a project unrelated to the current manuscript.

[8]Department of Pathology and Cell Biology, and the Herbert Irving Comprehensive Cancer Center, Columbia University, New York, NY, USA

Abstract

Although mutations in the RNA splicing factor SF3B1 are frequent in multiple cancers, their functional effects and therapeutic dependencies are poorly understood. Here we characterize 98 tumors and 12 isogenic cell lines harboring *SF3B1* hotspot mutations, identifying hundreds of cryptic 3' splice sites common and specific to different cancer types. Regulatory network analysis revealed that the most common *SF3B1* mutation activates MYC via effects conserved across human and mouse cells. *SF3B1* mutations promote decay of transcripts encoding the PP2A phosphatase subunit PPP2R5A, increasing c-MYC S62 and BCL2 S70 phosphorylation which, in turn, promote MYC protein stability and impair apoptosis, respectively. Genetic PPP2R5A restoration or pharmacologic PP2A activation impaired SF3B1-mutant tumorigenesis elucidating a therapeutic approach to aberrant splicing by mutant SF3B1.

Keywords

Alternative splicing; FTY-720; MYC; PPP2R5A; SF3B1

INTRODUCTION

Mutations in genes encoding RNA splicing factors occur across a variety of hematologic malignancies and solid tumors, and have provided evidence for the importance of aberrant splicing to tumorigenesis (1). Mutations in the core RNA splicing factor *SF3B1* are the most common across cancer types and occur as "hotspot" heterozygous point mutations. *SF3B1* hotspot mutations are amongst the most common genetic alterations in patients with myelodysplastic syndromes (MDS) (2, 3), chronic lymphocytic leukemia (CLL) (4, 5), and uveal melanoma (UVM) (6–8), and are also seen in 1–3% of many solid tumors, including breast invasive carcinoma (BRCA) and skin cutaneous melanoma (SKCM) (1). Analysis of the effects of *SF3B1* mutations on RNA splicing have consistently identified that these mutations promote usage of aberrant branchpoint residues, which most commonly manifests in transcripts bearing aberrant intron-proximal 3' splice site (3'ss) (9, 10). To date however, very few individual mis-spliced transcripts which functionally link mutant SF3B1 to malignant transformation have been identified. In addition, multiple distinct residues of SF3B1 are affected by hotspot mutations and many of these mutations exhibit cancer lineage specificity. For example, mutations at the arginine 625 residue of SF3B1 are strongly associated with uveal, acral, and mucosal melanomas (6, 11) whereas mutations at position K700 are present across myeloid leukemias, CLL, and epithelial cancers (12). However, mechanistic differences between distinct hotspot mutations in SF3B1 are not well defined nor is the basis for the cancer-specificity of SF3B1 mutant alleles understood.

It is expected that functional changes associated with *SF3B1* mutations are the result of aberrant splicing events in key genes leading to deregulation in activity of regulatory networks. For example, recent work identified robust aberrant splicing of the mRNA encoding the bromodomain protein BRD9 across cancer types and across individual hotspot mutations in *SF3B1* (13). However, the consequences of *SF3B1* mutations on dysregulated gene expression, which poorly overlap with the mRNAs mis-spliced by mutant SF3B1 (9, 10), are not well defined. To this end, here we performed an analysis of the impact of mutant SF3B1 on the activity of gene regulatory networks, which may be distinct from aberrant splicing changes associated with mutant SF3B1. In so doing we elucidate the effects of *SF3B1* hotspot mutations across cancer lineages at the level of both mRNA splicing and expression. This effort identified a striking effect of *SF3B1* mutations on post-translational regulation of multiple proteins with very well-established roles in tumorigenesis via inactivation of a specific regulatory subunit of the PP2A phosphatase complex. The partial inactivation of PP2A by aberrant splicing of a regulatory subunit illuminated a potential therapeutic strategy for *SF3B1* mutant malignancies via reactivation of residual PP2A activity.

RESULTS

Pan-cancer analysis identified differential splicing events based on lineage and *SF3B1* mutant allele

To provide a more complete understanding of how *SF3B1* mutations alter splicing globally, we performed a comprehensive pan-cancer analysis using computational approaches that enable the identification and quantification of alternative 3’ss with enhanced sensitivity. To this end, we collected RNA-seq data from 98 tumors and 12 isogenic cell lines harboring *SF3B1* hotspot mutations in the C-terminal HEAT repeat domains together with 102 randomly chosen *SF3B1* wild-type (WT) controls (Fig. 1A; Supplementary Table S1; Methods). Hotspot mutations mostly clustered into two specific residues within SF3B1’s HEAT repeat domains (Fig. 1A). The most frequent hotspot, K700E, was the most common mutation in CLL, MDS, acute myeloid leukemia (AML), and BRCA while mutations at position R625 were mostly restricted to UVM and SKCM. All the E902K/G variants were exclusively observed in bladder urothelial carcinoma (BLCA) whereas K666 mutations were present across multiple tumor types. The association of specific *SF3B1* mutational hotspots with distinct tumor types suggests the potential for allele-specific splicing abnormalities and unique pathogenic roles of each *SF3B1* mutational hotspot within each lineage of cancer. To examine this possibility, unsupervised hierarchical clustering was applied to the identified aberrant 3’ss sites (Fig. 1B and Supplementary Table S2). Unsupervised clustering clearly separated *SF3B1* mutant from *SF3B1* WT samples, with the exception of all TCGA BLCA (E902K/G) as well as one sarcoma case (TCGA SARC, D894H), suggesting that these specific mutations do not lead to aberrant 3’ss usage. In addition, the clustering dendrogram substructure revealed a difference in aberrant 3’ss usage between hematologic malignancies and solid tumors, as well as obvious tumor lineage specificity (Fig. 1B; Supplementary S1A; Chi-squared test; *P*-value = 4.33e-51). For instance, *SF3B1* mutated CLL patients clustered together despite coming from three independent cohorts and further grouped with another cluster consisting of AML, MDS, K562 cells, and Nalm-6 cells, indicating greater similarity in aberrant 3’ss usage among hematologic malignancies. Meanwhile, UVM and SKCM formed a stable subgroup, exhibiting a different splicing pattern from TCGA BRCA patients. At the same time, unsupervised clustering also demonstrated distinct preference of cryptic 3’ss associated with each mutational hotspot (Supplementary Fig. S1A; Chi-squared test; *P*-value = 1.40e-16). Consistent with our previous observation, clustering by rows demonstrated that splicing events split into two groups, mainly dominated by events associated with K700E (CLL and others) and R625 mutations (UVM and SKCM), respectively. In addition, we applied a principal component analysis (PCA) to the same data matrix of aberrant 3’ss usage, which indicated a more distinct separation of samples harboring mutations affecting the K700 and R625 residues of SF3B1 (Supplementary Fig. S1B).

Most cryptic 3’ss were associated with a modest change of Percent-Spliced-In (PSI) between *SF3B1* mutant and WT tumors, usually less than 10% (10). As previously reported, the distance from cryptic 3’ss to canonical site showed a striking peak around 10–30 bp upstream exon (9) (Supplementary Fig. S1C). Further evaluation of cryptic 3’ss usage specific to each mutational hotspot suggested that the distribution of distances from the canonical to the cryptic 3’ss varies among the different hotpots with altered sequence motif associated with the aberrant 3’ss (Fig. 1C; Supplementary Fig. S1D and S1E). For example, *SF3B1*$^{\mathrm{R625}}$ mutations seem to be associated with a shorter (< 25 bp) and more specific insertion, while K666N induces usage of longer inclusions. Accordingly, the sequence contexts associated with the cryptic 3’ss exclusive to *SF3B1*$^{\mathrm{R625}}$ are characterized by an upstream adenine enrichment, which was not observed in *SF3B1*$^{\mathrm{K666N}}$-specific cryptic 3’ss (Supplementary Fig. S1D). We next compared the cryptic 3’ss with differential usage between *SF3B1*$^{\mathrm{K700E}}$ (MDS, BRCA and CLL) and *SF3B1*$^{\mathrm{R625}}$ (UVM and SKCM) (Fig. 1D; Supplementary Methods). This analysis identified a list of cryptic 3’ss events that are probably specific to different *SF3B1* mutational hotspots, suggesting that K700E and R625 positions may have a differential preference of 3’ss usages.

We extended the above pan-cancer analyses of the effects of mutant splicing factors to established hotspot mutations in *SRSF2* and *U2AF1*. We identified 52 *SRSF2* mutant samples (including 29 *SRSF2*$^{\mathrm{P95}}$ mutant samples), as well as 59 *U2AF1* mutant samples (5 *U2AF1*$^{\mathrm{Q157}}$ and 32 *U2AF1*$^{\mathrm{S34F}}$ mutant samples) (Supplementary Fig. S2A; Supplementary Table S3). Analysis of the effects of these mutations on splicing identified that most of the alternative splicing events in *SF3B1* mutant samples were classified into alternative 3’ss, while the predominant events in *SRSF2* or *U2AF1* mutant samples were cassette exons (Supplementary Fig. S2B), which suggested the uniqueness of mutant SF3B1’s role in promoting cryptic 3’ss usage. Next, unsupervised hierarchical clustering was performed on all *SF3B1*, *SRSF2* and *U2AF1* mutant samples, by combining the previously identified significantly differential splicing events (Supplementary Fig. S2C). Consistent with our previous observation, *SF3B1* hotspot mutations were separated from *SRSF2* and *U2AF1* with exception of very few R625 mutants (UVM). In contrast, *SRSF2* and *U2AF1* mutant samples had less distinguishable splicing patterns from one another. Overall, these pan-cancer analyses suggested the singularity of the aberrant splicing pattern in *SF3B1* mutants.

Given the splicing specificity of *SF3B1* hotspot mutations, we performed gene set enrichment analysis (GSEA) against curated MSigDb gene sets to identify tumor- and *SF3B1* mutation-specific cellular processes. When we compared all the *SF3B1* mutant and WT samples across all 12 tumor types, significantly enriched gene sets included those involved in nonsense-mediated decay (NMD) (core enriched genes: a set of ribosomal genes), DNA repair (*POLL*, *ERCC8*, *POLB*, etc.) and RNA polymerase II initiation (*CDK7*, *TAF9*, *TAF12*, etc.) (Fig. 1E; Supplementary Table S4). We also identified differential enrichment of signaling pathways depending on *SF3B1* mutation and tumor types, including activation of NOTCH signaling in *SF3B1* mutant CLL (14) and heme metabolism and NF-κB signaling (core enriched genes: proteasome genes) in *SF3B1* mutant MDS patients (Supplementary Table S4) (15, 16). In addition, activation of multiple oncogenic pathways such as ERK/MAPK, mTOR, and apoptosis-related pathway was suggested in *SF3B1* mutant tumorigenesis (Supplementary Table S4). In contrast, we identified GO terms (enriched with mis-spliced genes) associated with RNA processing, cellular metabolism, and organophosphate biosynthesis in *SRSF2* mutant samples, and macromolecule catabolism, cellular metabolism, establishment of protein localization, and metabolism in *U2AF1* mutant samples (Supplementary Fig. S3A–S3C).

Activation of MYC signaling in *SF3B1* mutant chronic lymphocytic leukemia

To understand the functional role of mutant SF3B1 in promoting tumorigenesis from the view of transcriptional and post-translational interaction networks, we adopted a well-assembled transcriptional molecular interaction network developed in human B-cells (17) and performed a regulatory network analysis on *SF3B1* mutated CLL patients. In total, 721 differentially expressed genes between *SF3B1* mutant and WT samples from the ICGC cohort (Supplementary Table S5) were used as input to test the enrichment of each transcription factor (TF) network targets. When taking into account the direction of transcriptional changes, the top master regulator and the only statistically significant TF was MYC (hypergeometric test, q-value = 1.76e-07 for positive regulation, q-value = 4.12e-03 for negative regulation) (Fig. 2A; Supplementary Methods). This direction-specific association was validated from an independent dataset of 294 CLL patients from ICGC CLLE-ES project (Fig. 2B). We further confirmed this by a pre-ranked GSEA analysis as well as unsupervised clustering (Fig. 2C and 2D). When repeating the analysis on additional cancer types including UVM, SKCM, and BRCA, similar enrichment of MYC transcriptional program was detected in TCGA BRCA samples with *SF3B1*$^{\mathrm{K700E}}$ mutations, while it was absent in UVM and SKCM samples with *SF3B1*$^{\mathrm{R625}}$ mutations, or AML, lung adenocarcinoma, pancreatic adenocarcinoma, and uterine corpus endometrial carcinoma samples with *SRSF2*/*U2AF1* hotspot mutations (Supplementary Table S6). Taken together, these observations suggested that tumors harboring *SF3B1*$^{\mathrm{K700E}}$ mutations (and potentially mutations affecting H662, K666, and G742) activate the MYC transcriptional program.

SF3B1 mutations promote c-Myc-driven lymphomagenesis

We next sought to verify the effects of c-Myc activation by mutant Sf3b1 in the B-cell lineage *in vivo*. To achieve this, we crossed *Cd19*-cre$^{+/-}$ mice with conditional *Sf3b1*$^{\mathrm{K700E/+}}$ knock-in mice (18) to generate *Cd19*-cre$^{+/-}$ *Sf3b1*$^{\mathrm{K700E/+}}$ mice. Detailed analysis revealed that there are no robust changes in spleen weight, blood cell counts, lineage commitment, and B-cell maturation in *Sf3b1*$^{\mathrm{K700E/+}}$ mice compared to WT counterparts (Supplementary Fig. S4A–S4M). Next, *Cd19*-cre$^{+/-}$ *Sf3b1*$^{\mathrm{K700E/+}}$ mice were crossed to mice transgenic for *c-Myc* driven by the *IgH* enhancer (*Eμ-Myc* mice) (19) to generate control (*Cd19*-cre$^{+/-}$), *Sf3b1*$^{\mathrm{K700E}}$ mutant (*Cd19*-cre$^{+/-}$ *Sf3b1*$^{\mathrm{K700E/+}}$), *Eμ-Myc* (*Cd19*-cre$^{+/-}$ *Eμ-Myc*$^{\mathrm{Tg/+}}$), and *Sf3b1*$^{\mathrm{K700E}}$ *Eμ-Myc* double-mutant (*Cd19*-cre$^{+/-}$ *Sf3b1*$^{\mathrm{K700E/+}}$ *Eμ-Myc*$^{\mathrm{Tg/+}}$) mice

(Supplementary Fig. S5A). While *Cd19*-cre$^{+/-}$ *Sf3b1*$^{\mathrm{K700E/+}}$, *Cd19*-cre$^{+/-}$ *Eμ-Myc*$^{\mathrm{Tg/+}}$, and *Cd19*-cre$^{+/-}$ control mice did not develop B-cell malignancies within 300 days, four of eight *Sf3b1*$^{\mathrm{K700E/+}}$ *Eμ-Myc*$^{\mathrm{Tg/+}}$ double-mutant mice developed B-cell leukemia/lymphoma (Fig. 3A; Supplementary Fig. S5B). In serial transplantation into sublethally irradiated recipients, mice transplanted with *Cd19*-cre$^{+/-}$ *Sf3b1*$^{\mathrm{K700E/+}}$ *Eμ-Myc*$^{\mathrm{Tg/+}}$ double-mutant cells developed severe anemia, thrombocytopenia, and splenomegaly, resulting in significantly shorter survival compared to single-mutant or control mice (Fig. 3B–3H). These data provide the first evidence that *SF3B1* mutations contribute to tumorigenesis *in vivo*.

To understand the molecular mechanisms for c-MYC activation across *SF3B1* mutant cells and our mouse model, we next analyzed RNA-seq data from CLL patients, isogenic Nalm-6 cells, and sorted splenic B-cells from recipient mice (Supplementary Fig. S5C–S5E). This revealed a significant overlap in aberrant 3'ss events in *SF3B1* mutant CLL samples, Nalm-6 cells, and murine B-cells (Fig. 4A–4D; Supplementary Fig. S5F and S5G; Supplementary Table S7–S9). Most of these aberrant 3'ss events were validated by RT-PCR in both CLL patient samples and isogenic Nalm-6 cells and resulted in decreased protein levels (Fig. 4E and 4F; Supplementary Fig. S6A–S6F). Given that c-MYC activation was observed specifically in *SF3B1* mutant CLL and BRCA where mutations predominantly affect the K700 residue, we hypothesized that aberrant 3'ss usage specific to *SF3B1*$^{\mathrm{K700E}}$ mutant cancers might be responsible for c-MYC activation. Interestingly, mRNA expression levels of *c-MYC* were not elevated in *SF3B1* mutant CLL, BRCA, or Nalm-6 cells compared to *SF3B1*$^{\mathrm{WT}}$ counterparts and *SF3B1* mutant samples did not harbor MYC amplification (Supplementary Fig. S7A–S7E). These observations led us to hypothesize that MYC activation in *SF3B1*$^{\mathrm{K700E}}$ mutant cancers might occur via post-transcriptional and/or post-translational mechanisms. Among genes whose product has previously been shown to result in increased stability of c-MYC protein (20–22), *PPP2R5A* was the only gene whose aberrant splicing events were specifically observed in *SF3B1* K700E, H662D, and K666N mutant cells and were validated in human and mouse *SF3B1* mutant cells (Fig. 4F; Supplementary Fig. S6D–S6F). In addition, mis-splicing in *PPP2R5A* was more robust in *SF3B1*$^{\mathrm{K700E}}$ mutant CLL compared to that in *SF3B1*$^{\mathrm{R625}}$ mutant UVM (Supplementary Fig. S7F). These results led us to focus on the roles of PPP2R5A loss in c-MYC activation in more detail.

Aberrant splicing of *PPP2R5A* leads to c-MYC and BCL2 activation via post-translational modification

PPP2R5A is a regulatory B-subunit of the major serine-threonine phosphatase protein phosphatase 2A (PP2A) protein complex (which consists of a core trimer between the scaffolding A subunit, catalytic C subunit, and a regulatory B subunit (reviewed in ref.(23)). PP2A complex containing PPP2R5A dephosphorylates serine 62 (S62) of c-MYC, resulting in an unstable, singly threonine 58 (T58)-phosphorylated form of c-MYC that is a substrate for ubiquitination by FBXW7 and degradation by the 26S proteasome (20). As expected, aberrant *PPP2R5A* transcript was confirmed to result in NMD (Fig. 4G and 4H) and a decrease in PPP2R5A mRNA and protein expression was observed, which was associated with c-MYC upregulation in *SF3B1*$^{\mathrm{K700E}}$ mutant CLL, Nalm-6 cells, and mouse splenic B-cells (Fig. 4I–4K; Supplementary Fig. S7G–S7J; Supplementary Table S10–S11). Among genes encoding regulatory B subunit family members, *PPP2R5A* was specifically mis-spliced and down-regulated in *SF3B1* mutant tumors compared to WT counterparts across cancers (Fig. 4L; Supplementary Fig. S8A–S8G). The half-life of PPP2R5A protein was also diminished in *SF3B1* mutant cells (Supplementary Fig. S8H) although the mechanism for this is unknown. Consistent with the dramatic increase of S62-phosphorylated form of c-MYC in *SF3B1* mutant cells compared to that in WT cells (Fig. 4L; Supplementary Fig. S8I and S8J), *SF3B1*$^{\mathrm{K700E}}$ expression significantly decreased the rate of c-MYC protein degradation following inhibition of protein synthesis with cycloheximide (Fig. 4M). In contrast, there was no difference in MYC protein synthesis rate between *SF3B1* WT and mutant cells (Supplementary Fig. S8K). Importantly, restoration of PPP2R5A expression in *SF3B1* mutant cells almost completely reduced phosphorylation levels of c-MYC at S62, leading to protein degradation (Fig. 4N). To further evaluate the role of MYC phosphorylation, we utilized S62 mutant forms of MYC that either mimic (S762D) or prevent (S62A) MYC S62 phosphorylation. When we overexpressed HA-tagged c-MYC WT, S62A, or S62D in *SF3B1*$^{\mathrm{WT}}$ and *SF3B1*$^{\mathrm{K700E}}$ cells, S62A mutants significantly shortened MYC half-life while S62D mutants prolonged MYC half-life in both *SF3B1*$^{\mathrm{WT}}$ and *SF3B1*$^{\mathrm{K700E}}$ cells. These data are consistent with our observations that the differential status of S62 phosphorylation of c-MYC between *SF3B1*$^{\mathrm{WT}}$ and *SF3B1*$^{\mathrm{K700E}}$ cells altered MYC protein stability (Supplementary Fig. S8L).

We were further interested in potential BCL2 involvement in the context of c-MYC activation in mutant SF3B1-mediated tumorigenesis program because (i) serine 70 (S70)-phosphorylated form of BCL2 is another target of PPP2R5A (24), (ii) phosphorylation at S70 is required for BCL2’s anti-apoptotic function (25), and (iii) BCL2 has been shown to play a role in blocking c-MYC induced apoptosis (26, 27). We first verified that the S70-phosphorylated BCL2 is increased in *SF3B1* mutant cells compared to WT cells, which was canceled by PPP2R5A restoration (Fig. 4L and 4N). Intriguingly, mRNA expression of pro-apoptotic BH3-only BCL2 family genes such as *BAD*, *BIK*, *BMF*, and *BBC3* (*PUMA*) were decreased in *SF3B1* mutant Nalm-6 cells (Fig. 5A–5E; Supplementary Table S10), suggesting that S70-phosphorylated BCL2-mediated anti-apoptotic function coupled with transcriptional downregulation of pro-apoptotic BCL2 family might contribute to anti-apoptotic effect of c-MYC. Consistent with this, *SF3B1* mutant cells were more resistant to apoptotic stimulus, such as induced by a topoisomerase inhibitor, camptothecin (CPT) (Fig. 5F–5H). To evaluate the role of BCL2 phosphorylation, we utilized S70 mutant forms of BCL2 that either mimic (S70E) or prevent (S70A) BCL2 S70 phosphorylation (24). Expression of BCL2 S70E cDNA significantly protected *SF3B1*$^{\mathrm{WT}}$ cells from CPT-induced apoptosis and enhanced cell growth while BCL2 S70A expression had minimal effects compared to BCL2 WT. On the other hand, expression of BCL2 S70A induced more apoptosis upon treatment with CPT in *SF3B1*$^{\mathrm{K700E}}$ cells, resulting in inhibition of cell growth (Fig. 5I; Supplementary Fig. S9A–S9C). Next, we investigated how BCL2 phosphorylation enhances anti-apoptotic functions. Protein half-life of BCL2 WT, S70A, and S70E were almost identical, suggesting that BCL2 phosphorylation does not affect protein stability of BCL2 (Supplementary Fig. S9D). As BCL2 is known to bind BAK and antagonize the effects of BAK (which is required for mitochondrial permeabilization during apoptosis), we compared the binding affinity of either WT, S70A, or S70E BCL2 protein with BAK by immunoprecipitation assays following treatment with camptothecin for 5 hrs. This revealed that BCL2 S70E had higher binding affinity to BAK while BCL2 S70A had reduced affinity compared to BCL2 WT protein. These data suggest that BCL2 phosphorylation status at S70 regulates binding with BAK (Fig. 5J). Levels of cytochrome C release in the isogenic cell lines above were analyzed by intracellular flow cytometry following treatment with camptothecin for 5 hrs. Most likely as a result of BCL2 activation, cells with BCL2 S70A expression demonstrated a significantly increase in cytochrome C release compared to cells with BCL2 WT or S70E expression, which is consistent with our previous data that expression of BCL2 S70E cDNA significantly protected cells from CPT-induced apoptosis and enhanced cell growth while BCL2 S70A expression had minimal effects compared to BCL2 WT (Fig. 5K). Overall, these findings suggest that the mutant SF3B1-PPP2R5A axis regulates post-translational modification of BCL2 at S70 and plays an important role in the anti-apoptotic phenotype of *SF3B1* mutant cells.

Given that numerous mis-splicing events occur in the setting of mutant SF3B1, we next sought to evaluate the link among mutations in *SF3B1*, PPPR5A mis-splicing and expression, and MYC activity in more detail. We first evaluated the effects of restoring PPP2R5A levels in *Sf3b1*$^{\mathrm{K700E}}$ *Eμ-Myc* double-mutant tumors. We expressed an empty vector or PPP2R5a cDNA in *Cd19*-cre$^{+/-}$ *Sf3b1*$^{\mathrm{K700E/+}}$ *Eμ-Myc*$^{\mathrm{Tg/+}}$ tumors and transplanted these cells into recipients (Fig. 6A). Recipients transplanted with *Cd19*-cre$^{+/-}$ *Sf3b1*$^{\mathrm{K700E/+}}$ *Eμ-Myc*$^{\mathrm{Tg/+}}$ cells with restored PPP2R5A expression had lower WBC counts and less severe thrombocytopenia, splenomegaly, and tumor cell infiltration in multiple organs compared to control mice (Fig. 6B–6F). In addition, serial transplantation of *Sf3b1*$^{\mathrm{K700E/+}}$ *Eμ-Myc*$^{\mathrm{Tg/+}}$ tumor cells revealed that PPP2R5A overexpression significantly prolonged the survival (Fig. 6G). Conversely, depletion of PPP2R5A in *SF3B1* WT Nalm-6 cells enhanced phosphorylation of both c-MYC and BCL2, and conferred growth advantage *in vitro* (Supplementary Fig. S10A–S10C). Similarly, genetic depletion of Ppp2r5a in *Sf3b1*$^{\mathrm{WT}}$ *Eμ-Myc*$^{\mathrm{Tg/+}}$ tumors enhanced disease progression *in vivo* (Supplementary Fig. S10D–S10K). Overall, these data strongly suggest that alterations in PPP2R5A levels due to aberrant splicing by mutant SF3B1 promote MYC-driven tumorigenesis.

***SF3B1* mutant cells are preferentially sensitive to pharmacologic PP2A activation**

The molecular and functional consequences of loss of PPP2R5A-related c-MYC and BCL2 dephosphorylation suggested that activation of PP2A complex containing PPP2R5A regulatory B-subunit may be exploited for anti-tumor therapy. For this purpose, we assessed the therapeutic potential of the FDA-approved oral PP2A activator, FTY-720 (also known as fingolimod) (28–30). *SF3B1* mutant Nalm-6 cells were more sensitive to FTY-720 treatment than *SF3B1* WT counterparts, experiencing growth inhibition at lower concentration compared to *SF3B1* WT cells *in vitro* (Fig. 7A and 7B; Supplementary Fig. S11A–S11D). Similar results were obtained with other PP2A activators including the recently reported DT-061 (31, 32) as well as Perphenazine (PPZ) (33) *in vitro* (Supplementary Fig. S11E–S11H). Moreover, both S62-phosphorylated c-MYC and S70-phosphorylated BCL2 decreased in a dose-dependent manner upon treatment with FTY-720 (Fig. 7C). MYC protein half-life was shortened with FTY-720 treatment, which was accompanied by downregulation of gene expression of MYC target genes (Supplementary Fig. S11I and

S11J). In contrast, sensitivity to FTY-720 was diminished in *SF3B1* mutant cells with PPP2R5A overexpression (Supplementary Fig. S11K–S11M). Finally, to assess the efficacy of FTY-720 *in vivo*, we serially transplanted *Cd19*-cre$^{+/-}$ *Sf3b1*$^{+/+}$ or *Sf3b1*$^{K700E/+}$ mutant *Eμ-Myc*$^{Tg/+}$ tumors into sublethally irradiated Cd45.1^{+} recipient mice and treated these mice with either vehicle or FTY-720 (Fig. 7D). Similar levels of PP2A activation from *in vivo* FTY-720 treatment were seen in recipients of both *Sf3b1* WT and mutant tumors (Supplementary Fig. S12A and S12B). *Sf3b1*$^{K700E/+}$ *Eμ-Myc* tumors were more aggressive compared to *Sf3b1*$^{+/+}$ tumors as evidenced by elevated Cd45.2^{+} B-cells in PB, increased tumor burden in spleen and liver, increased Cd45.2 chimerism across organs, and worsened anemia and thrombocytopenia, consistent with the results above. However, FTY-720 treatment *in vivo* selectively improved these phenotypes in recipients of *Sf3b1*$^{K700E/+}$ *Eμ-Myc* tumors, diminished c-Myc expression and induced apoptosis to a greater extent in *Sf3b1*$^{K700E/+}$ *Eμ-Myc* tumors than in *Sf3b1*^{WT} *Eμ-Myc* tumors, and prolonged their survival while the effects on *Sf3b1*$^{+/+}$ *Eμ-Myc* tumors were minimal (Fig. 7E–7M; Supplementary Fig. S12C–S12G).

DISCUSSION

Despite abundant genetic data which suggest that mutations in *SF3B1* represent oncogenic drivers in malignancy, clear biological contribution of mutations in *SF3B1* to tumorigenesis has not been demonstrated. In fact, evaluation of the role of mutant versus WT alleles of *SF3B1* have failed to identify a role of these mutations in cancer maintenance and instead have highlighted the requirement of the WT allele in cells expressing heterozygous mutations in *SF3B1* (34). Here through combined evaluation of the effects of the *SF3B1* mutation on splicing, gene expression, and TF regulatory networks across cancer types, we identify a novel mechanism by which the mutant SF3B1-mediated co-transcriptional alterations in RNA splicing contribute to stabilization and activation of oncogenic MYC. Activation of the MYC pathway was molecularly conserved across human and mouse B-cell malignancy models and identifies a clear contribution of aberrant splicing driven by mutant SF3B1 to a biologic mechanism of tumorigenesis.

The high frequency of change-of-function mutations in *SF3B1* in cancer and the reliance of *SF3B1* mutant cells on otherwise WT splicing has resulted in efforts to target RNA splicing for therapeutic means in cells bearing mutations in *SF3B1* and other splicing factors. However, the clinical viability of targeting RNA splicing in patients is unclear and further efforts to dissect mechanistic dependencies in *SF3B1* mutant cells are needed. To this end, we identify that a specific enzymatic activity, PP2A phosphatase activity, is altered in *SF3B1* mutant cancers. PP2A's substrate specificity, function, and enzymatic activities are regulated in part by expression of specific regulatory B-subunits. Consistent with this, loss of specific regulatory B-subunits have been repeatedly shown to result in cellular transformation. Interestingly, the specific subunit of PP2A targeted for decay in SF3B1 mutant cells, PPP2R5A (also known as B56α), is well known to regulate human cell transformation from systematic RNAi screens for oncogenic PP2A regulators (35), studying PP2A targets of polyoma T antigens (which block interaction of B56 subunits with the PP2A holoenzyme) (36), and genetic depletion studies in mice (37). In fact, mice with hypomorphic for *Ppp2r5a* develop spontaneous skin tumorigenesis, lymphoid cell expansion, and increased clonogenic potential of hematopoietic precursors (37). Despite these abundant data highlighting PPP2R5A as a critical tumor suppressive subunit of PP2A however, genetic basis for loss of PPP2R5A in human cancers was absent until this current study.

One additional observation from this study was that distinct hotspot mutations in *SF3B1* have unique effects on RNA splicing and gene expression. For example, samples with mutations affecting the H4-H8 HEAT repeat domains of SF3B1 had much clearer effects on aberrant intron proximal 3’ splice site usage than samples with mutations at the D894 and E902 residues. Although the precise mechanistic basis for this is not clear yet, amino acid residues within HEAT repeat H4–H8 of SF3B1 are clustered in a small area and are exposed to solvent, suggesting that these mutations may disrupt SF3B1 interactions with other spliceosomal proteins or SF3b subunits (38) to induce aberrant branchpoint usage. In contrast, D894 and E902 residues are located at the H11 domain, which may not directly impact RNA interaction. These computational predictions will be important to evaluate in future functional studies which will likely require structural and biochemical evaluation of each mutant form of SF3B1 independently.

While prior work has highlighted MYC and BCL2 as critical substrates of PPP2R5A-containing PP2A, it is important to acknowledge that there are additional known substrates for this specific PP2A complex. Future work comprehensively defining the full spectrum of substrates of PPP2R5A-containing PP2A and how these are altered in *SF3B1* mutant cancers may therefore be very important. In addition, given the striking redundancy in B subunits of PP2A, where 15 genes encode 26 B subunits potentially assembling >100 distinct PP2A complexes, it will be important to determine how loss of PPP2R5A impacts other PP2A complexes in *SF3B1* mutant cells. Nonetheless, the striking redundancy in PP2A complexes allows for pharmacologic interventions to reactivate residual PP2A activity in *SF3B1* mutant tumors. Fingolimid (or FTY-720), the therapeutic modality used here, activates PP2A by binding SET, a negative regulator of PP2A, and directly causing its displacement from and assembly of active PP2A holo-enzymes (39). Our data highlight an important novel therapeutic approach targeting the impact of mutant SF3B1 on post-translational modification and stabilization of oncogenic MYC. The specific compound used here is far from the only means to reactivate PPP2R5A-containing PP2A, however, and future efforts to target *SF3B1* mutant tumors by complimentary means of reactivating via allosteric activation of its phosphatase activity may also be fruitful. Finally, besides *PPP2R5A*, recent studies identified robust alternative splicing changes in *BRD9* (13) and *DVL2* (14) that also play important roles in tumorigenesis of *SF3B1* mutant cancers. Aberrant 3’ss usage in these two genes were also observed in the current study (Supplementary Fig. S13A and S13B). The genetic effects of restoring PPP2R5A expression in *SF3B1* mutant tumors here, together with recent studies above, continues to highlight the need to study the impact of individual mis-splicing events generated by mutant SF3B1 to promote disease development.

METHODS

For complete experimental details and computational analyses, see also Supplementary Methods.

Pan-cancer *SF3B1* mutated sample collection and sequencing

RNA sequencing of patient samples or isogeneic cell lines with or without *SF3B1* hotspot mutations were collected from Columbia university medical center (CUMC), Memorial Sloan Kettering Cancer Center (MSKCC), and public portal resources including TCGA, ICGC dbGaP and GEO. Detailed sample information is shown in Supplementary Table S1.

Six chronic lymphocytic leukemia (CLL) patients with *SF3B1*$^{\mathrm{K700E}}$ mutation and six wild-type (WT) cases were identified from CUMC. This study is approved by the Institutional Review Boards of Columbia University, and performed in accordance with the Declaration of Helsinki. All patients gave their informed written consent. Poly-A pull-down was performed to enrich mRNA from total RNA samples, and libraries were prepared using the Illumina RNA TruSeqv2 PE100 60M (2 × 100 bp) and sequenced using the Illumina HiSeq2000 instrument at the Columbia Genome Center. Real-Time Analysis (RTA, Illumina) was used for base calling and bcl2fastq (version 1.8.4) for converting BCL to fastq format, coupled with adaptor trimming.

For TCGA RNA-seq data, we downloaded aligned bam files from cancer genomics cloud on November 2017 (cgc.sbgenomics.com). This cohort includes 16 uveal melanoma (UVM), 10 breast invasive carcinoma (BRCA), seven bladder urothelial carcinoma (BLCA), five skin cutaneous melanoma (SKCM), three acute myeloid leukemia (AML), two kidney renal clear cell carcinoma (KIRC), two liver hepatocellular carcinoma (LIHC), two prostate adenocarcinoma (PRAD), two sarcoma (SARC), and two thymoma (THYM) samples. In the meantime, equal number of WT samples were randomly chosen with the closest name id of TCGA barcode for each mutated sample.

The ICGC CLLE-ES cohort consists of six cases of *SF3B1*$^{\mathrm{K700E}}$, one *SF3B1*$^{\mathrm{G742D}}$, one *SF3B1*$^{\mathrm{H662D}}$, one *SF3B1*$^{\mathrm{K666N}}$ and nine randomly chosen WT samples. Raw fastq files were downloaded from ICGC Data Portal (https;//dcc.icgc.org) with the project name ‘CHRONIC LYMPHOCYTIC LEUKEMIA - ES’. Controlled access to these data is approved with application number: DACO-1023313. The sequencing data are paired-end 2 × 76 bp libraries.

In addition, we collected two human AML patients (K666N, R625C) as well as two WT samples from Leucegene datasets. Raw fastq files were downloaded from NCBI’s Sequence Read Archive (SRA; accession numbers GSE67039). Nine samples of *SF3B1* mutated Nalm-6 cell lines were also employed from GEO accession: GSE72790, together with three WT samples. Three cases of *SF3B1*$^{\mathrm{K700E}}$ K562 cells and three WT cells were downloaded from GEO accession: GSE95011 (40). Data from six *SF3B1* mutated (four K700E, one K666T, and one K666R) and six WT MDS patients were obtained from GEO accession: GSE85712 (18). Another cohort of 19 *SF3B1*$^{\mathrm{K700E}}$ MDS samples with the same number of randomly chosen WT samples were added from GSE114922 (41). Six *SF3B1*$^{\mathrm{K700E}}$ and one *SF3B1*$^{\mathrm{K666E}}$ case of CLL patients were accessed from dbGaP under the project of The UC San Diego CLL Study (phs000767.v1.p1).

Collectively, we have established transcriptomic characterization of Pan-cancer *SF3B1* mutations on 110 samples covered by 12 tumor types.

Identification of novel cryptic 3’splice site usage

In order to annotate novel 3’ss that are not present in current genome, we adopted the splice junction read output by STAR alignment (42). This preprocess is motivated by DeBoever et al. (10), to enable a more sensitive detection of novel sites, specifically designed for 3/5’ss identification. To this end, all the bam files were transformed back to .fastq format (samtools), and re-aligned using a splice junction database (10). Counts of junction reads from SJ.out.tab file (STAR output) were merged into a unique matrix, with each row indicates one splice junction and column for each sample. We further filtered out junctions with a read coverage of < 50 sum up across all samples. Then, for each junction, we defined it as a novel splice site if it only has one end (either 3’ or 5’) annotated in the provided known genome, while the other end is not. Corresponding canonical junction are found if it shares the same annotated end of the cryptic junction and the other end also annotated. If this kind of canonical junction did exist, we calculated the distance between the novel end and the corresponding canonical end. If there was more than one distance, we utilized the minimum. After adding the information of transcript’s strand and relative position to the canonical site, we determined whether a cryptic site is on 3’ss or 5’ss, upstream or downstream. For mouse RNA-Seq, we reproduced this essential preprocess using a standard mm10 genome (Ensembl: Mus_musculus. GRCm38.75). Junctions with both ends unannotated were discarded from the analysis.

Next, with clear relationship of each cryptic junction to its canonical one, we calculated the Percent-Spliced-In (PSI) using raw reads counts for each sample, transforming the reads matrix into a PSI matrix with values between 0–1. Then, for two groups of interested comparison, t-test was applied for all novel cryptic splice site using PSI, rather than reads counts, followed by BH multiple test correction. Difference of averaged PSI between two groups was also adopted as important metrics for potential differential splicing. A bar plot of $\log_2$ distance in base pair was used to demonstrate cryptic 3’ splicing pattern on significantly differentially used novel sites.

To compare aberrant 3’ss usage between human CLL and mouse B-cells, mouse genes were mapped into human symbols. A hypergeometric test was used to evaluate the significant level of overlapped common genes.

Patient Samples

Studies were approved by the Institutional Review Boards of CUMC and MSKCC and conducted in accordance to the Declaration of Helsinki protocol. Written informed consent was obtained from all participants.

Animals

All animals were housed at MSKCC. All animal procedures were completed in accordance with the Guidelines for the Care and Use of Laboratory Animals and were approved by the Institutional Animal Care and Use Committees at MSKCC. The number of mice in each experiment was chosen to provide 90% statistical power with a 5% error level. Generation and genotyping of the *Sf3b1*$^{\mathrm{K700E/+}}$ conditional knock-in mice on C57BL/6 background were as described (18). *Eμ-Myc* mice have been described previously (19). Complete blood count analysis was performed on PB collected from submandibular, using a Procyte Dx Hematology Analyzer (IDEXX Veterinary Diagnostics).

Bone marrow transplantation assays

Freshly dissected femurs and tibias were isolated from *Cd19*-cre$^{+/-}$, *Cd19*-cre$^{+/-}$ *Sf3b1*$^{K700E/+}$, *Cd19*-cre$^{+/-}$*Eμ-Myc*$^{Tg/+}$, *Cd19*-cre$^{+/-}$ *Sf3b1*$^{K700E/+}$ *Eμ-Myc*$^{Tg/+}$ Cd45.2^{+} mice. BM was flushed with a 3-cc insulin syringe into cold PBS supplemented with 2% bovine serum albumin to generate single-cell suspensions. BM cells were pelleted by centrifugation at 1,500 rpm for 4 min and red blood cells (RBCs) were lysed in ammonium chloride-potassium bicarbonate lysis (ACK) buffer for 3 min on ice. After centrifugation, cells were resuspended in PBS/2% BSA, passed through a 40μm cell strainer, and counted. For transplantation experiments, 1.0×10^6 BM cells from *Cd19*-cre$^{+/-}$, *Cd19*-cre$^{+/-}$ *Sf3b1*$^{K700E/+}$, *Cd19*-cre$^{+/-}$*Eμ-Myc*$^{Tg/+}$, *Cd19*-cre$^{+/-}$ *Sf3b1*$^{K700E/+}$ *Eμ-Myc*$^{Tg/+}$ Cd45.2^{+} mice were transplanted via tail-vein injection into 8-week old sublethally irradiated (450 cGy) Cd45.1^{+} recipient mice. For each bleeding, whole blood cell counts were measured on an automated blood analyzer.

FTY-720 treatment *in vivo* and measurement of PP2A activity

FTY-720 (Sigma Aldrich) was dissolved in water and administrated intraperitoneally (3 mg/kg/day). The dose was optimized and determined by multiple pilot tests to minimize weight loss (such that all mice maintained ≥85% of their weight after two weeks of treatment). Protein lysates extracted from the spleen of treated mice were assayed to evaluate the efficacy of FTY-720 to activate PP2A complex *in vivo,* using the PP2A Immunoprecipitation Phosphatase Assay kit as described by the manufacturer (Millipore Sigma).

mRNA stability assays

mRNA stability assay was performed as previously described (43). Briefly, anti-*UPF1* shRNA- or control shRNA lentivirus-infected Nalm-6 *SF3B1*$^{K700E/+}$ knock-in cells were generated by puromycin selection (1 μg/mL) for 7 days and shRNAs against *UPF1* were expressed by doxycycline (2 μg/mL) for 2 days. GFP (shRNA)-positive cells were FACS sorted, treated with 2.5 μg/ml Actinomycin D (Life Technologies), and harvested at 0, 2, 4, 8, and 12 hrs.

Metabolic labeling and capture of newly synthesized protein

This was done as previously described (44). Briefly, newly synthesized proteins were labeled using the Click-iT Protein Labeling kit (Invitrogen). Isogenic Nalm-6 cells were cultured in fresh medium for 24 hrs, washed twice with PBS, and resuspended in methionine-free RPMI 1640 medium (Gibco) supplemented with 10% FCS for 30 min, at which point the methionine analog L-azidohomoalanine (AHA; Invitrogen) was added (50 μM) to allow incorporation of AHA into nascent proteins. MG-132 (Sigma, M7449; 5 μM) was added at 4 hrs before the methionine replacement. Protein was extracted from the cells and 150 μg of total protein was used in the cross-linking of AHA-labeled nascent proteins to alkyne-derivatized biotin in Click-iT Protein Reaction Buffer (Invitrogen) according to the manufacturer's instructions. Biotin-cross-linked nascent protein was captured overnight with streptavidin-coated Dynabeads (M-280, Invitrogen) and eluted. The whole volume of AHA-labeled, biotin-cross-linked, streptavidin-precipitated protein was separated by SDS–PAGE.

Statistical analyses

Statistical significance was determined by (i) unpaired two-sided Student's t-test after testing for normal distribution, (ii) one-way or two-way ANOVA followed by Dunnett's, Tukey's, Sidak's, or Dunnett's multiple comparison test, or (iii) Kruskal-Wallis tests with Uncorrected Dunn's test where multiple comparisons should be adjusted (unless otherwise indicated). Data were plotted using GraphPad Prism 7 software as mean values, with error bars representing standard deviation.

Data availability

The data that support the findings of this study are available from the corresponding author upon reasonable request. The RNA sequencing data have been deposited in NCBI Sequence Read Archive (SRA) under accession number GSE116391.

Supplementary Material

Refer to Web version on PubMed Central for supplementary material.

Acknowledgments

We thank Esther A. Obeng and Benjamin L. Ebert for sharing *Sf3b1*^{K700E} conditional knock-in mice and Goutham Narla, Michael G. Kharas and Piro Lito for technical advice. Z.L. is supported by NIH grant P01CA087497. A. Yoshimi is supported by grants from the Aplastic Anemia and MDS International Foundation (AA&MDSIF), the Lauri Strauss Leukemia Foundation, and the Japanese Society for the Promotion of Science (JSPS) Overseas Research Fellowships. A. Yoshimi is supported by grants from the Aplastic Anemia and MDS International Foundation (AA&MDSIF), the Lauri Strauss Leukemia Foundation, and the Japanese Society for the Promotion of Science (JSPS) Overseas Research Fellowships. A. Yoshimi and S.C.-W. Lee. are supported by the Leukemia and Lymphoma Society Special Fellow Award. S.C.-W. Lee is supported by the NIH/NCI (K99 CA218896) and the American Society of Hematology (ASH) Scholar Award. O. Abdel-Wahab is supported by grants from NIH/NHLBI (R01 HL128239), the Dept. of Defense Bone Marrow Failure Research Program (W81XWH-16-1-0059), the Starr Foundation (I8-A8-075), the Henry & Marilyn Taub Foundation, the Edward P. Evans Foundation, Leukemia and Lymphoma Society, and the Pershing Square Sohn Cancer Research Alliance. R. Rabadan is supported by NIH grants (R01 CA185486, R01 CA179044, U54 CA193313 and U54 209997) and NSF/SU2C/V-Foundation Ideas Lab Multidisciplinary Team (PHY-1545805).

REFERENCES

1. Seiler M, Peng S, Agrawal AA, Palacino J, Teng T, Zhu P, et al. Somatic Mutational Landscape of Splicing Factor Genes and Their Functional Consequences across 33 Cancer Types. Cell Rep 2018;23:282–96 e4. [PubMed: 29617667]
2. Papaemmanuil E, Cazzola M, Boultwood J, Malcovati L, Vyas P, Bowen D, et al. Somatic SF3B1 mutation in myelodysplasia with ring sideroblasts. N Engl J Med 2011;365:1384–95. [PubMed: 21995386]
3. Yoshida K, Sanada M, Shiraishi Y, Nowak D, Nagata Y, Yamamoto R, et al. Frequent pathway mutations of splicing machinery in myelodysplasia. Nature 2011;478:64–9. [PubMed: 21909114]
4. Quesada V, Ramsay AJ, Lopez-Otin C. Chronic lymphocytic leukemia with SF3B1 mutation. N Engl J Med 2012;366:2530. [PubMed: 22738114]

5. Wang L, Lawrence MS, Wan Y, Stojanov P, Sougnez C, Stevenson K, et al. SF3B1 and other novel cancer genes in chronic lymphocytic leukemia. N Engl J Med 2011;365:2497–506. [PubMed: 22150006]
6. Furney SJ, Pedersen M, Gentien D, Dumont AG, Rapinat A, Desjardins L, et al. SF3B1 mutations are associated with alternative splicing in uveal melanoma. Cancer Discov 2013;3:1122–9. [PubMed: 23861464]
7. Harbour JW, Roberson ED, Anbunathan H, Onken MD, Worley LA, Bowcock AM. Recurrent mutations at codon 625 of the splicing factor SF3B1 in uveal melanoma. Nat Genet 2013;45:133–5. [PubMed: 23313955]
8. Martin M, Masshofer L, Temming P, Rahmann S, Metz C, Bornfeld N, et al. Exome sequencing identifies recurrent somatic mutations in EIF1AX and SF3B1 in uveal melanoma with disomy 3. Nat Genet 2013;45:933–6. [PubMed: 23793026]
9. Darman RB, Seiler M, Agrawal AA, Lim KH, Peng S, Aird D, et al. Cancer-Associated SF3B1 Hotspot Mutations Induce Cryptic 3’ Splice Site Selection through Use of a Different Branch Point. Cell Rep 2015;13:1033–45. [PubMed: 26565915]
10. DeBoever C, Ghia EM, Shepard PJ, Rassenti L, Barrett CL, Jepsen K, et al. Transcriptome sequencing reveals potential mechanism of cryptic 3’ splice site selection in SF3B1-mutated cancers. PLoS Comput Biol 2015;11:e1004105.
11. Martin M, Masshofer L, Temming P, Rahmann S, Metz C, Bornfeld N, et al. Exome sequencing identifies recurrent somatic mutations in EIF1AX and SF3B1 in uveal melanoma with disomy 3. Nature genetics 2013;45:933–6. [PubMed: 23793026]
12. Dvinge H, Kim E, Abdel-Wahab O, Bradley RK. RNA splicing factors as oncoproteins and tumour suppressors. Nat Rev Cancer 2016;16:413–30. [PubMed: 27282250]
13. Inoue D, Chew GL, Liu B, Michel BC, Pangallo J, D’Avino AR, et al. Spliceosomal disruption of the non-canonical BAF complex in cancer. Nature 2019; 574:432–6. [PubMed: 31597964]
14. Wang L, Brooks AN, Fan J, Wan Y, Gambe R, Li S, et al. Transcriptomic characterization of SF3B1 mutation reveals its pleiotropic effects in chronic lymphocytic leukemia. Cancer cell 2016;30:750–63. [PubMed: 27818134]
15. Lee SC, North K, Kim E, Jang E, Obeng E, Lu SX, et al. Synthetic Lethal and Convergent Biological Effects of Cancer-Associated Spliceosomal Gene Mutations. Cancer Cell 2018;34:225–41 e8. [PubMed: 30107174]
16. Yoshimi A, Abdel-Wahab O. Splicing factor mutations in MDS RARS and MDS/MPN-RS-T. Int J Hematol 2017;105:720–31. [PubMed: 28466384]
17. Lefebvre C, Rajbhandari P, Alvarez MJ, Bandaru P, Lim WK, Sato M, et al. A human B-cell interactome identifies MYB and FOXM1 as master regulators of proliferation in germinal centers. Molecular systems biology 2010;6:377. [PubMed: 20531406]
18. Obeng EA, Chappell RJ, Seiler M, Chen MC, Campagna DR, Schmidt PJ, et al. Physiologic Expression of Sf3b1(K700E) Causes Impaired Erythropoiesis, Aberrant Splicing, and Sensitivity to Therapeutic Spliceosome Modulation. Cancer Cell 2016;30:404–17. [PubMed: 27622333]
19. Adams JM, Harris AW, Pinkert CA, Corcoran LM, Alexander WS, Cory S, et al. The c-myc oncogene driven by immunoglobulin enhancers induces lymphoid malignancy in transgenic mice. Nature 1985;318:533–8. [PubMed: 3906410]
20. Yeh E, Cunningham M, Arnold H, Chasse D, Monteith T, Ivaldi G, et al. A signalling pathway controlling c-Myc degradation that impacts oncogenic transformation of human cells. Nat Cell Biol 2004;6:308–18. [PubMed: 15048125]
21. Arnold HK, Sears RC. Protein phosphatase 2A regulatory subunit B56alpha associates with c-myc and negatively regulates c-myc accumulation. Mol Cell Biol 2006;26:2832–44. [PubMed: 16537924]
22. Mori K, Maeda Y, Kitaura H, Taira T, Iguchi-Ariga SM, Ariga H. MM-1, a novel c-Myc-associating protein that represses transcriptional activity of c-Myc. J Biol Chem 1998;273:29794–800. [PubMed: 9792694]
23. Perrotti D, Neviani P. Protein phosphatase 2A: a target for anticancer therapy. Lancet Oncol 2013;14:e229–38. [PubMed: 23639323]

24. Ruvolo PP, Clark W, Mumby M, Gao F, May WS. A functional role for the B56 alpha-subunit of protein phosphatase 2A in ceramide-mediated regulation of Bcl2 phosphorylation status and function. J Biol Chem 2002;277:22847–52. [PubMed: 11929874]
25. Deng X, Gao F, Flagg T, May WS, Jr. Mono- and multisite phosphorylation enhances Bcl2's antiapoptotic function and inhibition of cell cycle entry functions. Proc Natl Acad Sci U S A 2004;101:153–8. [PubMed: 14660795]
26. Patel JH, McMahon SB. BCL2 is a downstream effector of MIZ-1 essential for blocking c-MYC-induced apoptosis. J Biol Chem 2007;282:5–13. [PubMed: 17082179]
27. Wagner AJ, Small MB, Hay N. Myc-mediated apoptosis is blocked by ectopic expression of Bcl-2. Mol Cell Biol 1993;13:2432–40. [PubMed: 8455620]
28. Matsuoka Y, Nagahara Y, Ikekita M, Shinomiya T. A novel immunosuppressive agent FTY720 induced Akt dephosphorylation in leukemia cells. Br J Pharmacol 2003;138:1303–12. [PubMed: 12711631]
29. Brinkmann V, Davis MD, Heise CE, Albert R, Cottens S, Hof R, et al. The immune modulator FTY720 targets sphingosine 1-phosphate receptors. J Biol Chem 2002;277:21453–7. [PubMed: 11967257]
30. Chiba K. FTY720, a new class of immunomodulator, inhibits lymphocyte egress from secondary lymphoid tissues and thymus by agonistic activity at sphingosine 1-phosphate receptors. Pharmacol Ther 2005;108:308–19. [PubMed: 15951022]
31. Kauko O, O'Connor CM, Kulesskiy E, Sangodkar J, Aakula A, Izadmehr S, et al. PP2A inhibition is a druggable MEK inhibitor resistance mechanism in KRAS-mutant lung cancer cells. Sci Transl Med 2018;10.
32. Tohme R, Izadmehr S, Gandhe S, Tabaro G, Vallabhaneni S, Thomas A, et al. Direct activation of PP2A for the treatment of tyrosine kinase inhibitor-resistant lung adenocarcinoma. JCI Insight 2019;4.
33. Gutierrez A, Pan L, Groen RW, Baleydier F, Kentsis A, Marineau J, et al. Phenothiazines induce PP2A-mediated apoptosis in T cell acute lymphoblastic leukemia. J Clin Invest 2014;124:644–55. [PubMed: 24401270]
34. Zhou Q, Derti A, Ruddy D, Rakiec D, Kao I, Lira M, et al. A chemical genetics approach for the functional assessment of novel cancer genes. Cancer Res 2015;75:1949–58. [PubMed: 25788694]
35. Sablina AA, Hector M, Colpaert N, Hahn WC. Identification of PP2A complexes and pathways involved in cell transformation. Cancer research 2010;70:10474–84. [PubMed: 21159657]
36. Chen Y, Xu Y, Bao Q, Xing Y, Li Z, Lin Z, et al. Structural and biochemical insights into the regulation of protein phosphatase 2A by small t antigen of SV40. Nat Struct Mol Biol 2007;14:527–34. [PubMed: 17529992]
37. Janghorban M, Langer EM, Wang X, Zachman D, Daniel CJ, Hooper J, et al. The tumor suppressor phosphatase PP2A-B56alpha regulates stemness and promotes the initiation of malignancies in a novel murine model. PloS one 2017;12:e0188910.
38. Cretu C, Schmitzova J, Ponce-Salvatierra A, Dybkov O, De Laurentiis EI, Sharma K, et al. Molecular Architecture of SF3b and Structural Consequences of Its Cancer-Related Mutations. Mol Cell 2016;64:307–19. [PubMed: 27720643]
39. Saddoughi SA, Gencer S, Peterson YK, Ward KE, Mukhopadhyay A, Oaks J, et al. Sphingosine analogue drug FTY720 targets I2PP2A/SET and mediates lung tumour suppression via activation of PP2A-RIPK1-dependent necroptosis. EMBO Mol Med 2013;5:105–21. [PubMed: 23180565]
40. Seiler M, Yoshimi A, Darman R, Chan B, Keaney G, Thomas M, et al. H3B-8800, an orally available small-molecule splicing modulator, induces lethality in spliceosome-mutant cancers. Nature medicine 2018;24:497.
41. Pellagatti A, Armstrong RN, Steeples V, Sharma E, Repapi E, Singh S, et al. Impact of spliceosome mutations on RNA splicing in myelodysplasia: dysregulated genes/pathways and clinical associations. Blood 2018:blood-2018-04–843771.
42. Dobin A, Davis CA, Schlesinger F, Drenkow J, Zaleski C, Jha S, et al. STAR: ultrafast universal RNA-seq aligner. Bioinformatics 2013;29:15–21. [PubMed: 23104886]

43. Yoshimi A, Lin KT, Wiseman DH, Rahman MA, Pastore A, Wang B, et al. Coordinated alterations in RNA splicing and epigenetic regulation drive leukaemogenesis. Nature 2019;574:273–7. [PubMed: 31578525]

44. Vu LP, Prieto C, Amin EM, Chhangawala S, Krivtsov A, Calvo-Vidal MN, et al. Functional screen of MSI2 interactors identifies an essential role for SYNCRIP in myeloid leukemia stem cells. Nat Genet 2017;49:866–75. [PubMed: 28436985]

SIGNIFICANCE

Here we identify that mutations in *SF3B1,* the most commonly mutated splicing factor across cancers, alter splicing of a specific subunit of the PP2A serine/threonine phosphatase complex to confer post-translational MYC and BCL2 activation, which is therapeutically intervenable using a FDA-approved drug.

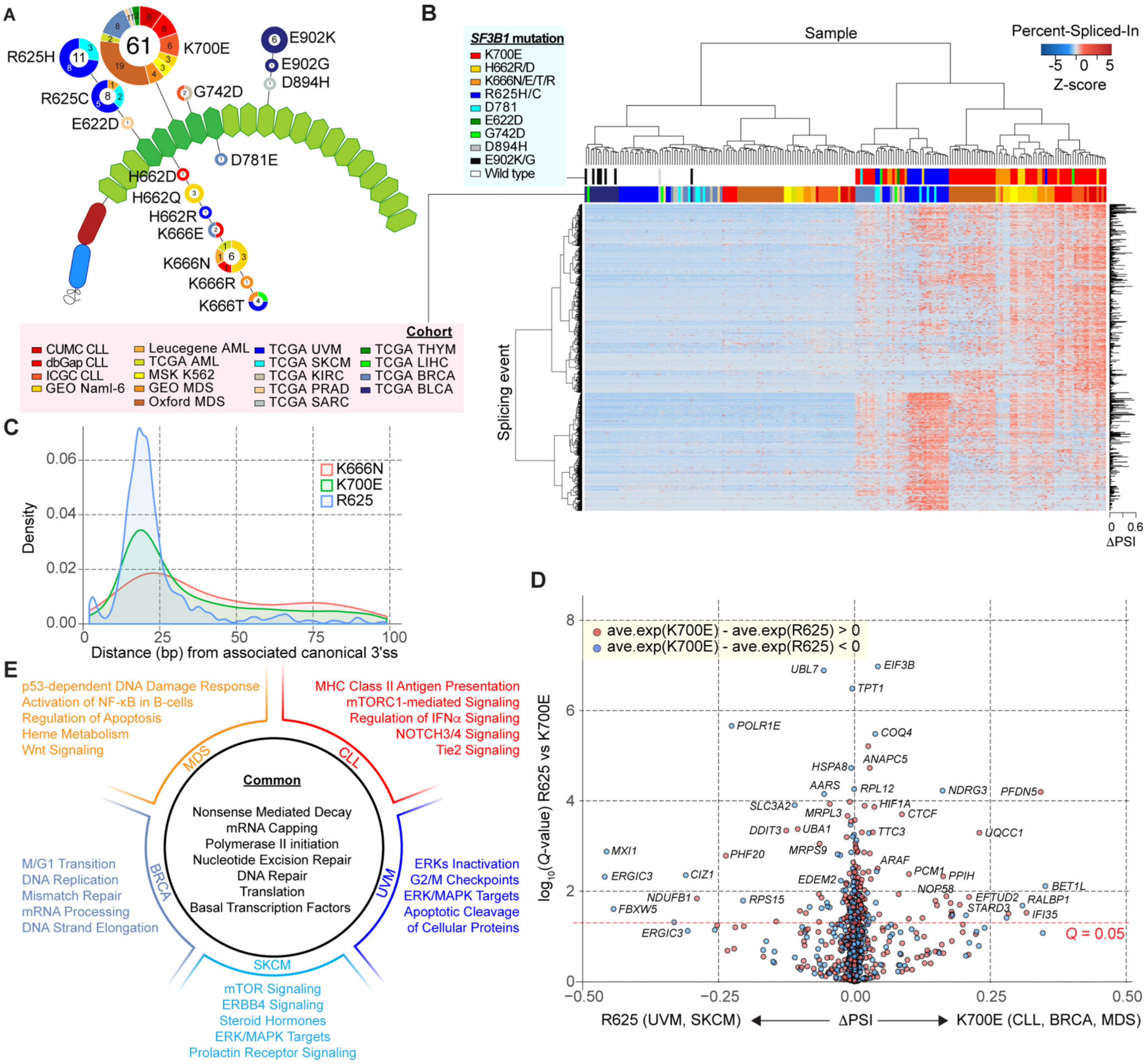

Figure 1.

Differential aberrant splicing events across *SF3B1* mutant cancers. **A,** Location and frequency of *SF3B1* hotspot mutations from the pan-cancer dataset on the HEAT repeat domains (green hexagons) of SF3B1. The numbers in the center/on the edge of each circle denote the sample size of each mutation across all/specific to each cohort (see Supplementary tables for abbreviations). **B,** Hierarchical clustering and heatmap analysis of differential 3’ splice sites (3’ss) between *SF3B1* mutant and wild-type (WT) samples. Rows and columns represent cryptic 3’ss events and samples, respectively. 1,401 cryptic 3’ss identified from the Pan-cancer dataset are shown. Z-score in the matrix represents normalized Percent-Spliced-In (PSI). **C,** Density plot of distance in base pairs from associated canonical 3’ss to cryptic 3’ss. **D,** Volcano plot representation of differentially spliced changes between *SF3B1*$^{\mathrm{K700E}}$ mutations (CLL, BRCA and MDS) and *SF3B1*$^{\mathrm{R625}}$ mutations (UVM and SKCM) showing the magnitude (difference of PSI; x-axis) and significance (-$\log_{10}$(*q*-value); y-axis). **E,** Representative gene sets significantly enriched in gene set enrichment analysis (GSEA) comparing all *SF3B1* mutant and WT samples, as well as the results from comparisons done within each cancer type.

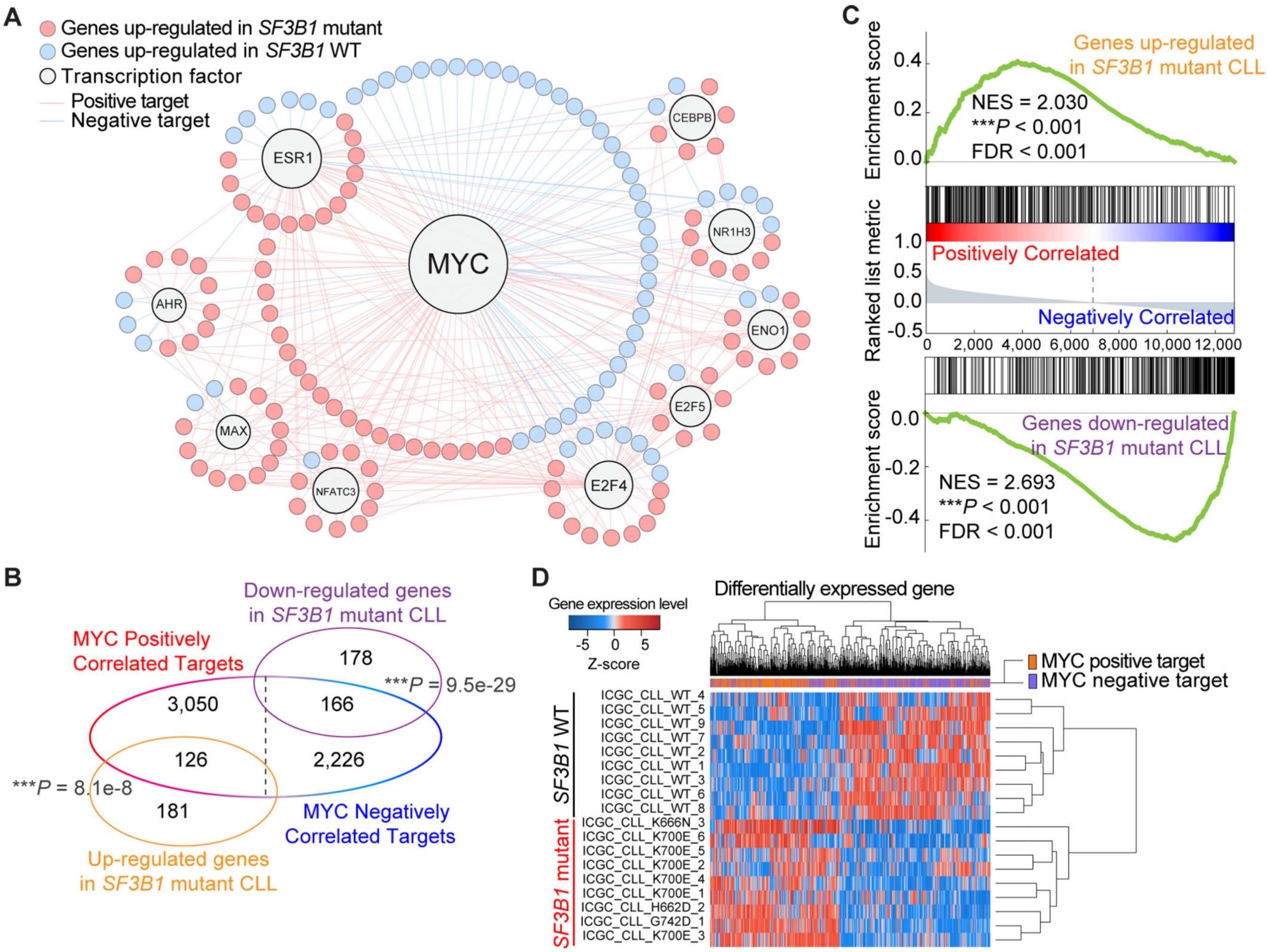

Figure 2.

Activation of MYC signaling in *SF3B1* mutant chronic lymphocytic leukemia (CLL). **A,** Transcriptional regulation network of significantly enriched master regulators. Nodes indicate transcription factors or target genes differentially expressed between *SF3B1* mutant and WT CLL. **B,** Venn diagram showing the overlap of MYC targets and differentially expressed genes in *SF3B1* mutant samples (hypergeometric test; $P = 8.1e\text{-}08$ for positive regulated genes; $P = 9.5e\text{-}29$ for negative regulated genes). **C,** Results of pre-ranked GSEA enrichment analysis on MYC target genes. Genes up/down-regulated in *SF3B1* mutant CLL were tested against a pre-ranked gene list which was generated based on the correlation with MYC. **D,** Heatmap of unsupervised clustering of differentially expressed genes based on *SF3B1* genotype. Analyses in **B**, **C**, and **D** were performed using an expression matrix of 294 CLL patients from ICGC Data Portal (Z-score > 0 represents upregulation in *SF3B1* mutant samples). $^{***}P < 0.001$.

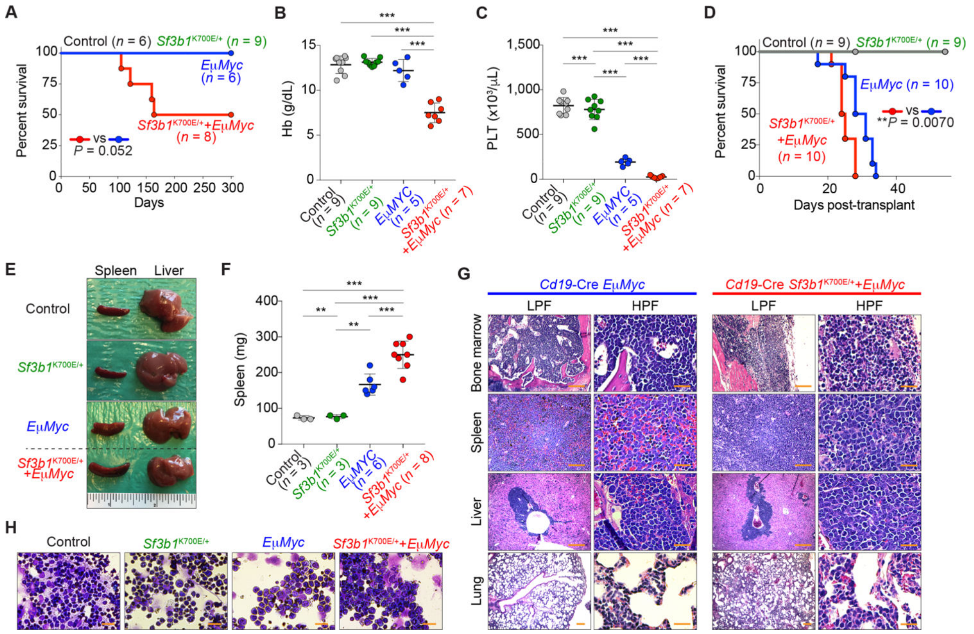

Figure 3.

SF3B1 mutations promote c-Myc-driven lymphomagenesis. **A** and **D,** Kaplan-Meier curves of survival of primary (**A**) and recipient (**D**) mice transplanted with bone marrow (BM) cells from mice with indicated genotype (Log-rank (Mantel-Cox) test). **B** and **C,** Hemoglobin (Hb) (**B**) and platelet (PLT) (**C**) counts of recipient mice at day 28 post-transplant (the mean value ± SD is shown). **E** and **F,** Representative pictures of spleen and liver of recipient mice (**E**) (an inch ruler is shown together) and spleen weights of recipient mice (**F**) at day 28 (*Cd19*-Cre$^{+/-}$ control and *Cd19*-Cre$^{+/-}$ *Sf3b1*$^{\mathrm{K700E/+}}$ mice were sacrificed for comparison; the mean value ± SD is shown). **G,** Hematoxylin and eosin (H&E) of tissues from representative moribund primary mice (scale bar 200 μm: Low power field (LPF); 50 μm: High power field (HPF)). **H,** Representative cytomorphology of BM mononuclear cells of recipient mice (scale bar 20 μm). $^{**}P < 0.01$; $^{***}P < 0.001$.

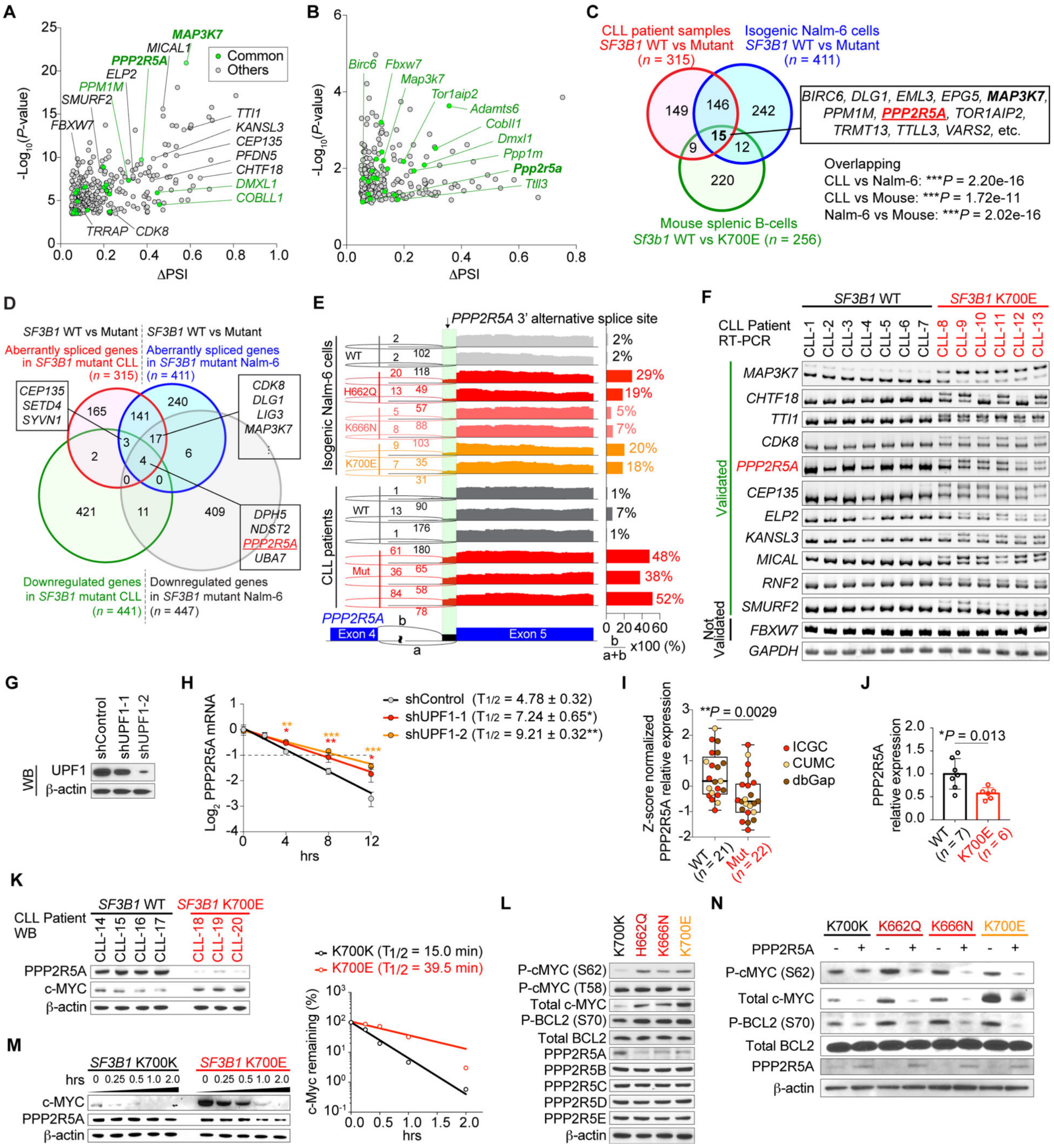

Figure 4.

Aberrant splicing of *PPP2R5A* leads to c-MYC activation via post-translational regulation. **A** and **B,** (Half-) Volcano plot showing alternative 3'ss events in *SF3B1* mutant CLL (**A**) and mouse *Sf3b1*$^{\text{K700E}}$ splenic B-cells (**B**). Genes highlighted in green represent genes that are mis-spliced in both human *SF3B1* mutant CLL and mouse *Sf3b1*$^{\text{K700E}}$ splenic B-cells. **C,** Venn diagram of numbers of differentially spliced genes in indicated datasets (Fisher's exact, test). **D,** Venn diagram of numbers of differentially spliced and down-regulated genes in *SF3B1* mutant CLL and Nalm-6 samples. **E,** Sashimi plots of *PPP2R5A* 3'ss in isogenic

Nalm-6 cells (top) and representative CLL samples (bottom) with or without *SF3B1* mutations. **F,** Representative RT-PCR results of aberrantly spliced transcripts in BM samples from CLL patients with or without *SF3B1* mutations. **G,** Western blot (WB) analysis of Nalm-6 *SF3B1*$^{\mathrm{K700E}}$ knock-in cells transduced with shRNAs against UPF1 (representative results from three biologically independent experiments with similar results). **H,** Half-life of PPP2R5A transcripts with alternative 3'ss were measured by qPCR ($n = 3$; the mean value ± SD is shown; *P*-values* compared to shControl). **I,** Boxplot of *PPP2R5A* expression from CLL patients with or without *SF3B1* mutations based on RNA-seq data (sources indicated with different colors; the mean value ± SD is shown). **J** and **K,** Quantitative real-time PCR (**J**) and WB (**K**) analysis of primary CLL patient samples with or without *SF3B1* mutations (the mean value ± SD is shown). **L** and **N,** WB analysis of protein lysates from isogenic Nalm-6 cells (representative results from three independent experiments are shown). **M,** Isogenic Nalm-6 cells were treated with 100 μg/mL cycloheximide (CHX) and cell lysates were prepared at the indicated time points after treatment. The amount of c-MYC protein at each time point (left) was quantified using ImageJ and protein half-life was calculated using Prism 7 (right). *$P < 0.05$; ** $P < 0.01$; *** $P < 0.001$.

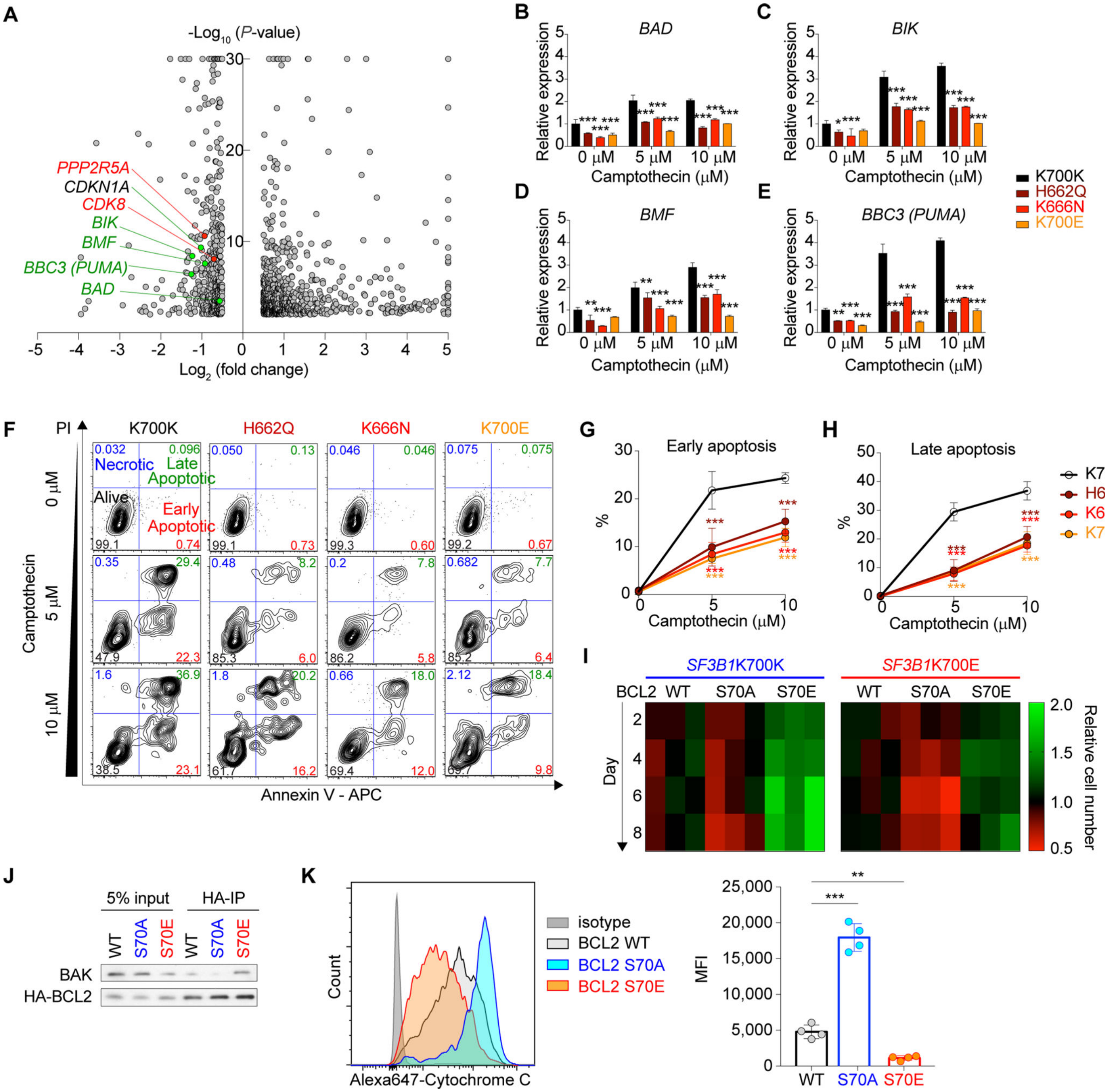

Figure 5.

Impaired apoptosis in *SF3B1* mutant cells linked to increased BCL2 S70 phosphorylation. **A,** Volcano plot showing differentially expressed genes in isogenic *SF3B1* mutant Nalm-6 cells (|Log$_2$ (Fold change) | = 0.5 and -log$_{10}$(P-value) = 2 are used as thresholds; genes with |x| > 5 and/or y > 30 are shown on |x| = 5 or y = 30). **B-E,** qPCR of BAD (**B**), BIK (**C**), BMF (**D**), and BBC3 (PUMA) (**E**) in isogenic Nalm-6 cells upon treatment with camptothecin at indicated concentrations for 5 hrs (n = 3; the mean value ± SD is shown; P-values are shown for comparisons of K700K versus each mutant). **F,** Representative flow cytometry analysis of isogenic Nalm-6 cells upon treatment with camptothecin for 5 hrs. **G** and **H,** Percentages of cells in early (Annexin V+ PI-; top) (**G**) and late (Annexin V+ PI-; bottom) (**H**) apoptotic phases with different concentrations of camptothecin ($n = 3$; the mean value ± SD is shown; P-values are shown for comparisons of K700K versus each mutant). **I,** Heatmap was made using Prism 7 based on the cell growth upon camptothecin treatment at 1 μM ($n = 3$; scale represents the relative cell number at each day relative to BCL2 WT expressing cells). **J,** Parental Nalm-6 cells were transduced with either WT, S70A, or S70E BCL2 (all HA-tagged), treated with 5 μM camptothecin for 5 hrs, and protein lysates were immunoprecipitated with an HA antibody. Eluted protein (95% was used for BAK blotting and 5% was used for HA blotting) as well as 5% input protein were analyzed by WB. **K,** Isogenic Nalm-6 cells from **J** were treated with 5 μM camptothecin for 5 hrs and cytochrome C release was evaluated by intracellular flow cytometry staining (left; representative flow cytometry analysis from four independent experiments; Mean fluorescence intensity (MFI) is provided on the right; $n = 4$; the mean ± SD). $*P < 0.05$; $**P < 0.01$; $***P < 0.001$.

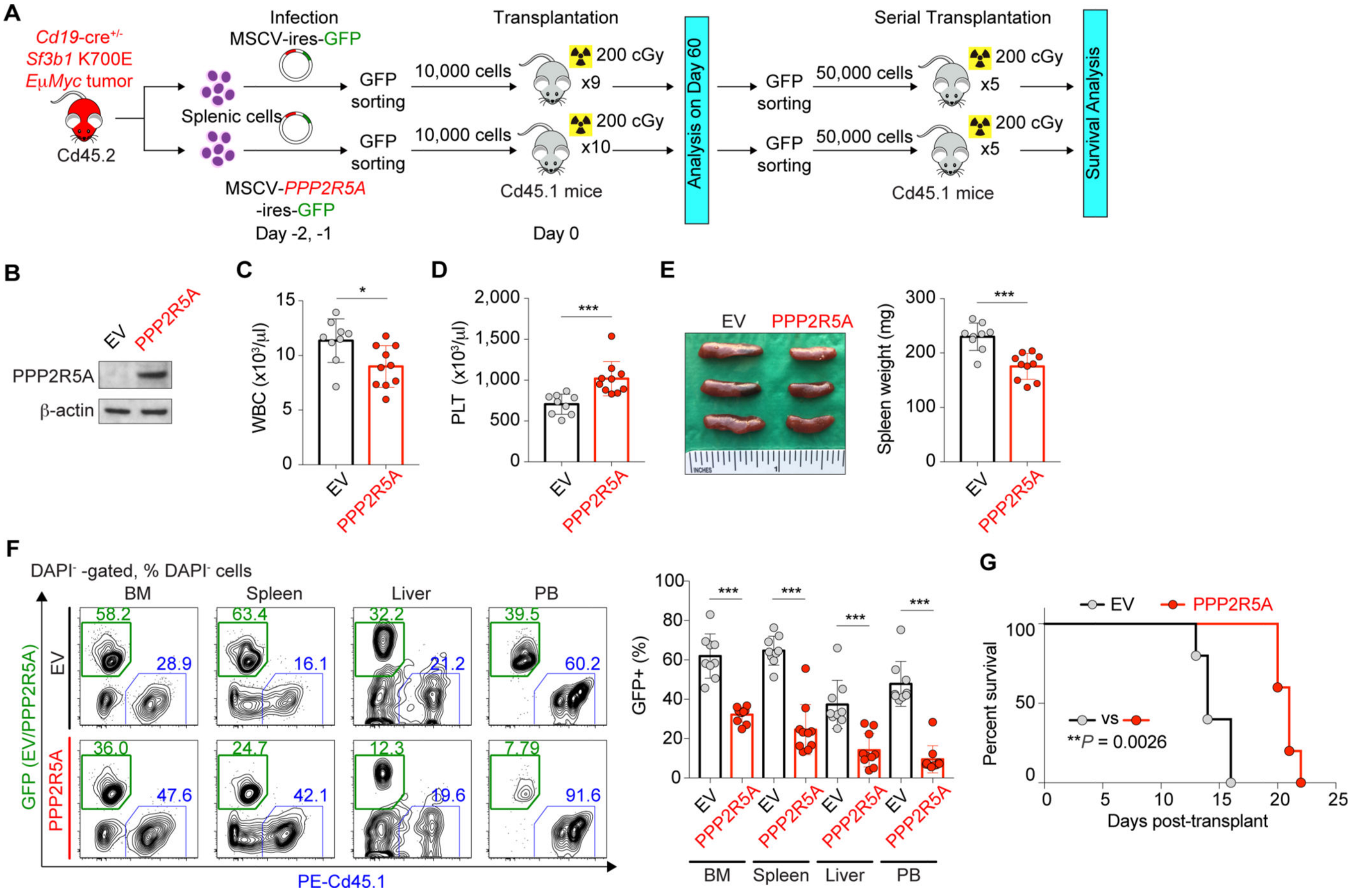

Figure 6.

Restoration of PPP2R5A expression in *Sf3b1* mutant *Eμ-Myc* tumors reduces tumorigenicity. **A,** Schematic representation of the study design. **B,** Confirmation of PPP2R5A expression in *Cd19*-cre$^{+/-}$ *Sf3b1*$^{K700E/+}$ *Eμ-Myc*$^{Tg/+}$ cells with expression of an empty vector (EV) or PPP2R5A cDNA. **C** and **D,** WBC (**C**) and PLT (**D**) counts of recipients (the mean value ± SD is shown). **E,** Representative photo of spleen (left) and spleen weight of recipients (right; the mean value ± SD is shown; an inch ruler is shown together). **F,** Percentages of GFP^{+} DAPI^{-} cells in BM, spleen, liver, and PB (right) with representative flow cytometry analysis (left) (the mean value ± SD is shown). **G,** Kaplan-Meier curves of survival of recipients transplanted with *Sf3b1*$^{K700E/+}$ *Eμ-Myc* tumor ± PPP2R5A expression (Log-rank (Mantel-Cox) test). *$P < 0.05$; **$P < 0.01$; ***$P < 0.001$.

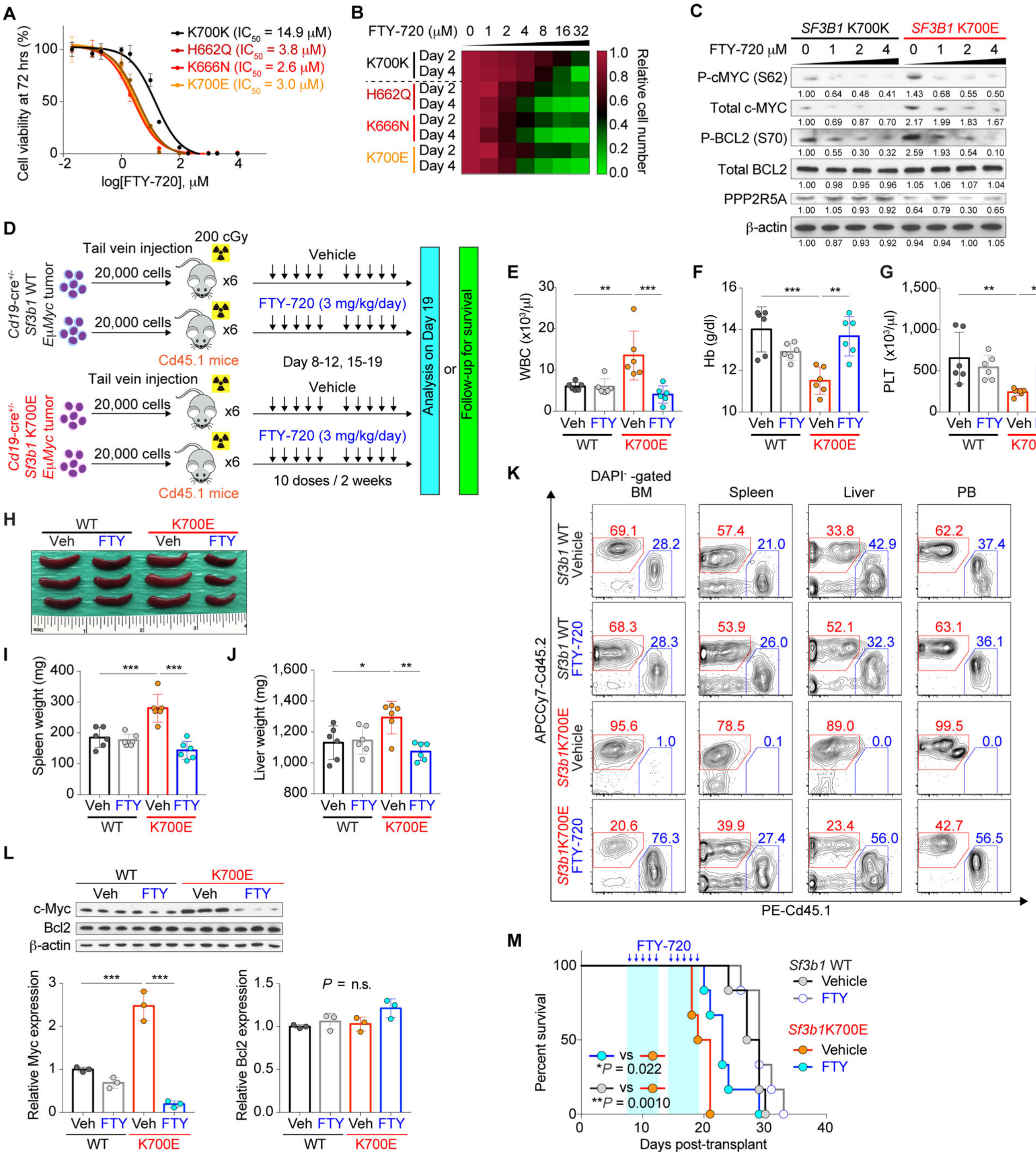

Figure 7.

Preferential sensitivity of *SF3B1* mutant cells to PP2A reactivation. **A,** Dose response curves of isogenic Nalm-6 cells to FTY-720 ($n = 3$; the mean value ± SD is shown). IC_{50} value for each genotype is indicated. **B,** Heatmap was made using Prism 7 based on the cell growth upon FTY-720 treatment with increasing doses ($n = 3$; scale represents the relative cell number at each dose of FTY-720 relative to vehicle-treated cells with 2 or 4 days of FTY-720 treatment). **C,** WB analysis of protein lysates from isogenic Nalm-6 cells treated with FTY-720 at various concentrations for 24 hrs (representative results from three independent experiments are shown). **D,** Schematic representation of the study design. **E-G,** WBC (**E**), Hb (**F**), and PLT (**G**) counts of mice ($n = 6$ per genotype; the mean value ± SD is shown). **H-J,** Representative photo of spleens (**H**) and weight of spleen (**I**) and liver (**J**) in recipients ($n = 6$ per genotype; the mean value ± SD is shown; an inch ruler is shown together). **K**, Representative flow cytometry analysis of Cd45.2$^+$ DAPI$^-$ cells in BM, spleen, liver, and PB (quantification of %Cd45.2$^+$ DAPI$^-$ cells is shown in Supplementary Fig. S12C–S12F). **L,** Cd45.2$^+$B220$^+$ splenic cells from **D** at day 19 were FACS-sorted and analyzed (top; 3 mice per group; $n = 1$ experiment). The amount of Myc and Bcl2 protein was quantified using ImageJ (bottom; the mean value ± SD). **M,** Kaplan-Meier curves of survival of recipient mice treated with either vehicle or FTY-720 ($n = 5$ per genotype; treatment period is marked in light blue; Log-rank (Mantel-Cox) test). $^*P < 0.05$; $^{**}P < 0.01$; $^{***}P < 0.001$.